Electronic Supplementary Material (ESI) for RSC Advances.

Electronic Supplementary Information for

Mapping the effect of geometry on the radiative rate in core/shell QDs: Core size dictates the conduction band offset

Maxwell P. Hoffman,[1†] Autumn Lee, [1†] Nejc Nagelj,[1] Youjin V. Lee,[2] Jacob H. Olshansky[1]*

[1]Department of Chemistry, Amherst College, Amherst, MA 01002, USA

[2]Department of Chemistry, University of California, Berkeley, Berkeley, CA, 94703

Email: *jolshansky@amherst.edu

[†] Equal contribution

Contents

Synthesis

Chemicals: Trioctylphosphine oxide (TOPO, 99%), selenium (Se, 99.99 %), cadmium oxide (CdO, ≥ 99.99%), oleic acid (OA, 90%), 1-octadecene (ODE, 90%), oleylamine (OLAM, ≥ 98% primary amine), and 1-octanethiol (OctSH, ≥ 98.5%) were purchased from SigmaAldrich and used as received. Other chemicals used include tri-n-octylphosphine (TOP, 99%, STREM), octadecylphosphonic acid (ODPA, 99%, PCI Synthesis) and the anhydrous solvents acetone, isopropanol, and hexanes. Reagents were purchased at reagent grade and used as received unless otherwise noted.

CdSe core synthesis. The core QDs were synthesized based on a previously published procedure.[1,2] Briefly, 60 mg of CdO, 280 mg of ODPA, and 3 g of TOPO were combined in a 25 mL round-bottomed flask. The mixture was degassed under vacuum at 120 °C for 20 minutes and complexed at 320 °C under inert atmosphere until the solution turned clear and colorless. After complexation, 1 mL of TOP was injected. The reaction vessel was heated towards 380 °C, and a TOP-selenide (60 mg Se complexed with 0.5 mL TOP) solution was quickly injected upon reaching this temperature. After the injection, the reaction mixture was allowed to remain at elevated temperatures for a short period of time- less than 5 seconds for small cores and about 45 seconds for large cores— and then cooled quickly. The QDs were crashed out from the reaction mixture by centrifuging after addition of excess isopropanol. The QDS were then cleaned by cycles of resuspension in hexanes, and precipitation with isopropanol followed by centrifugation for 3 minutes at 8000 rpm. The hexane/isopropanol cleaning cycles were done about three times, and the final pellet was resuspended in hexanes and stored in inert atmosphere. Sizes and concentrations were determined following previously published empirical calibration.[3]

CdSe/CdS core/shell synthesis. The shelling reaction was adapted from previously published procedures.[2,4] About 100 nmol of the core QDs, 3 mL of ODE, and 3 mL of OLAM, were

combined in a 50 mL round-bottomed flask, attached to a bump trap, as the reaction bumped several times during the injection. The reaction solution was degassed, first at room temperature for 1 hr then at 120 °C for 30 min. The reaction mixture was then heated towards 310 °C under inert atmosphere. At 240 °C, the injection of a 0.2 M cadmium oleate solution in ODE and a 0.22 M OctSH solution in ODE was initiated. The injection rate was set to 3 mL/hr.

For the small core shelling reactions, the temperature was kept at 240 °C for the first 0.5 mL of each injection solution to prevent Ostwald ripening as small CdSe QDs that are not passivated with CdS shell may restructure. For shelling reactions of small cores, 10.5 mL of each injection solution was used to grow the QDs to a predicted 12.4 nm diameter. For medium core shelling reactions, 16.6 mL of each injection solution was used to grow to a predicted 14.3 nm diameter. For large core shelling reactions, 22.5 mL of each injection solution was used to grow to a predicted 15.3 nm diameter. The final diameter did not always match predictions since the exact amount of QD cores used varied between runs and varying volumes of aliquots were drawn out during the shelling process.

For each of the three core sizes, three shelling reactions were done. For each of these nine reactions, about 0.1 mL of five to six aliquots of QDs with different shell thickness were drawn out from the reaction while it was in progress. Photophysical measurements were made after filtering the aliquots in hexanes through a microfilter. Thirty minutes of annealing time was given between injection and aliquot removal to ensure moderate monodispersity of the sample. Aliquots that were extracted too early in the injection stage exhibited low PLQY, presumably due to only a partial or thin coverage of the CdSe cores with CdS shell. All aliquots were kept under argon during the synthesis and optical measurements.

Electron microscopy

TEM sample were prepared by drop-casting the colloidal QDs of appropriate concentration on CF400-Cu grids (Electron Microscopy Sciences). Images were acquired on a FEI Tecnai T20 with a LaB6 filament and 200 kV accelerating voltage. TEM images were taken for each aliquot and were processed with a Matlab program described previously to obtain the average diameter and standard deviation of the QDs.[5,6] With this program, more than 500 nanoparticles were analyzed for each aliquot. The standard deviations in diameter serve as our horizontal error for radiative rate vs. diameter plots such as in main text Figure 3 (d,e, and f)

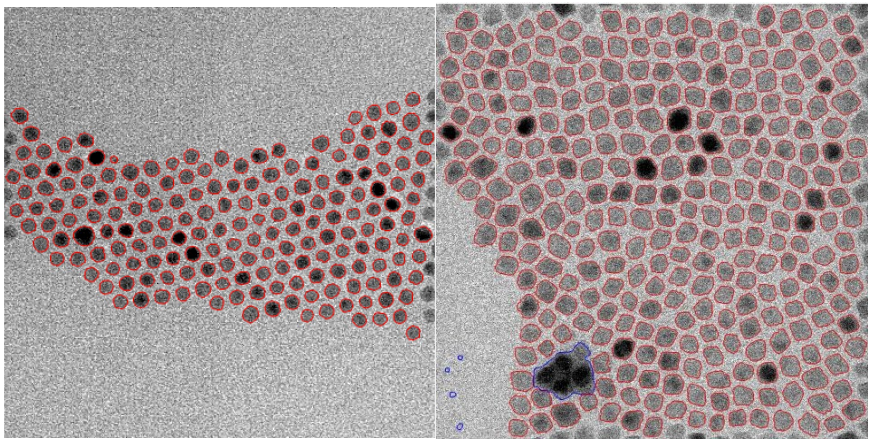

Figure S1. TEM images of two different samples. Red outline shows the selected area for the measurement of average diameter.

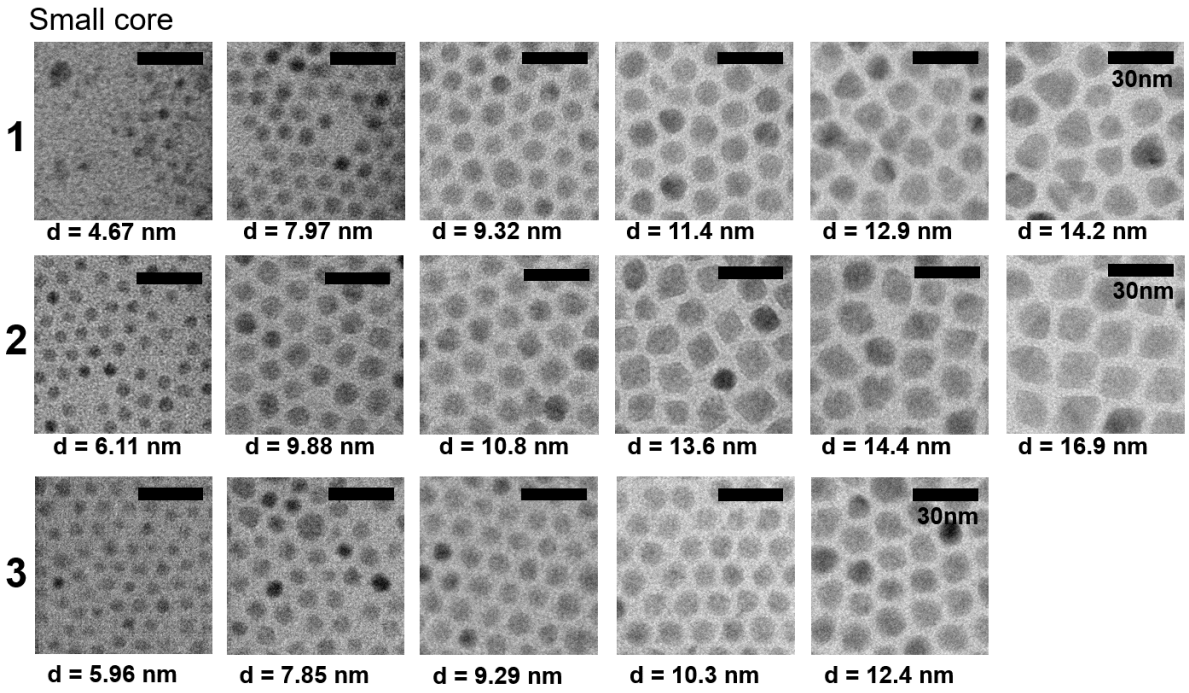

Figure S2. TEM images of all core/shell QDs analyzed from the small cores.

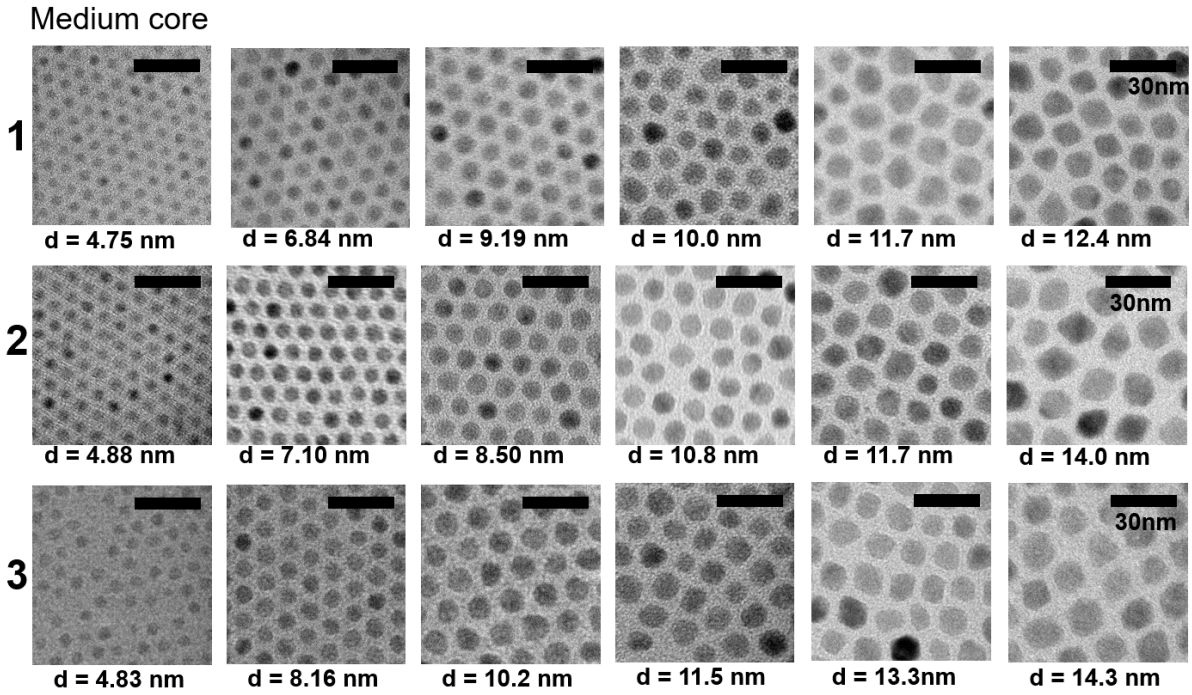

Figure S3. TEM images of all core/shell QDs analyzed from the medium cores.

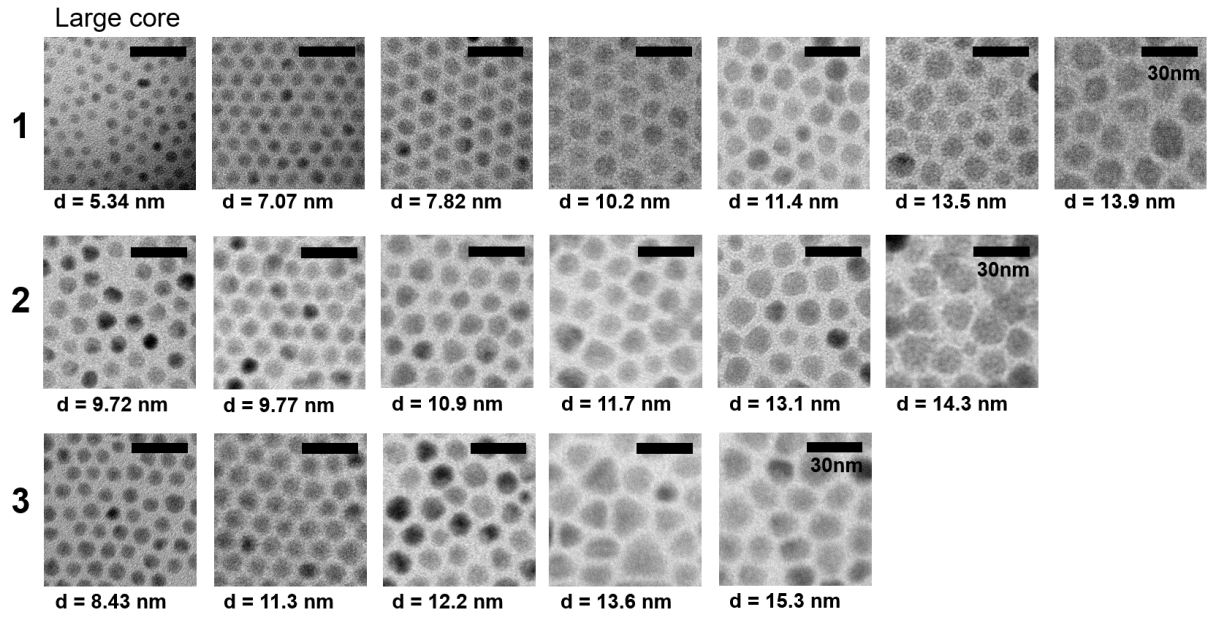

Figure S4. TEM images of all core/shell QDs analyzed from the large cores.

Optical spectroscopy

All optical measurements were performed on particles dispersed in hexanes. Absorption spectra were collected on a Shimadzu 3600 spectrophotometer. Photoluminescence emission spectra were collected on a Horiba Jobin Yvon TRIAX 320 Fluorolog. Quantum yield measurements were performed by referencing to Rhodamine 6G in absolute Ethanol, as described previously.[7] Photoluminescence lifetime measurements were acquired using a Picoquant Fluotime 300 spectrometer, a PMA 175 detector, and an LDH-P-C-405 diode laser with a 407 nm excitation wavelength.

Effective Mass Modelling

Our mathematical model of the quantum dots models them as spheres, which we then solve the Schrödinger equation in spherical coordinates, such that our wavefunction solution is as follows:

$$\psi(r,\theta,\phi) = R(r)\Upsilon(\theta,\phi) \quad \text{S1}$$

The angular component, $\Upsilon(\theta,\phi)$, depends primarily on the angular momentum quantum number l and the magnetic quantum number m_l. For the purposes of our model, we only study the quantum dots in their lowest energy state, with $l = 0$, which produces a constant angular component $\Upsilon(\theta,\phi) = \sqrt{\frac{1}{4\pi}}$. What is left is the radial component $R(r)$:

$$\frac{d}{dr}\left(r^2\frac{dR}{dr}\right) - \frac{2mr^2}{\hbar^2}[V(r) - E]R = l(l+1)R \quad \text{S2}$$

In which r is the radius, V is the potential energy, m is the mass, and E is the energy. This can be simplified by a change of variables:

$$u(r) \equiv rR(r) \quad \text{S3}$$

to become the radial equation (with $l = 0$):

$$-\frac{\hbar^2}{2m}\frac{d^2u}{dr^2} + uV(r) = Eu \quad \text{S4}$$

In our case, this calculation becomes more complicated since a core/shell quantum dot can be treated as a particle in a box (core), inside of another box (shell), inside of yet another box (ligand shell). As a result, our wavefunction becomes split into three distinct regions where the

electron carries both a different effective mass and a different potential energy, each of which is different from the same values for the hole. Our method of choice for tackling this problem was the finite difference method. This method of calculating the wavefunction is ideal for us since it allows us more flexibility with a high degree of accuracy compared to analytical methods, which are decidedly more complicated when dealing with multiple shells and a variable effective mass. The wavefunction can be solved analytically by solving a system of $2N - 2$ linear equations for the wavefunction, where N represents the number of regions inside the QD.[8]

The Schrödinger Equation at a given position r is defined using the finite difference method:

$$\widehat{H}\psi_r = (V_r + 2t)\psi_r - t\psi_{r-1} - t\psi_{r+1} \qquad \text{S5}$$

where ψ_r is the wavefunction at r, V_r is the potential energy at r, and t is a kinetic energy term, defined as:

$$t \equiv \frac{\hbar^2}{2m\Delta r^2} \qquad \text{S6}$$

However, since our model uses a variable effective mass, our term t is also variable as opposed to constant; as a result, we cannot define it before filling out our $\widehat{H}$-matrix and as a result, our function becomes more elaborate. In addition, the potential energy of an electron inside our QD changes from core to shell to ligand, so that portion of the equation also becomes variable. We defined our variables as such:

	Electron Effective Mass	Electron Potential (eV)	Hole Effective Mass	Hole Potential (eV)
CdSe	0.13	- 4.04	0.45	5.74
CdS	0.19	$0.475r_c^{-4} - 4.04$	0.8	6.34
Ligand	1.0	- 1.0	0.1	8.4

Table S1.

At first, we experimented with using a constant electron potential for CdS; however, as we applied the model to our experimental data, we realized that the best fit value for the conduction band offset depended on the size of the core. The theoretical curves in Figure 3 of the main text employ these core-size specific best fit conduction band offsets of 0.18, 0.04 and 0.0 eV for small, medium, and large cores. These core-size-dependent offsets prompted us to attempt to determine an empirical fit for the electron potential inside the CdS as a function of the core radius (r_c). This empirical fit is described in greater detail in the main text.

Returning to the steps involved in the calculations, our next step was calculating the $\widehat{H}$-matrix. Since our model uses a variable effective mass, we must specify boundary conditions for the positions at the start ($\widehat{H}_{0,0}$) and end ($\widehat{H}_{n,n}$) of the matrix. In addition, we need to define a way to transition from core to shell to ligand smoothly; to accomplish this, each value for *r* receives one of three effective electron masses, with points of *r* inside the core using the electron effective mass for CdSe, points inside the shell using the effective mass for CdS, and points in the ligand using the effective mass for an organic ligand (which is effectively 1). Potential energies are also defined in this way; each *r* point gets a unique potential based on whether that point is inside the core, shell, or ligand. This allows us to define the wavefunction in boundary cases where the point is right at the edge of the core, shell, or ligand, and allows for a continuous wavefunction.

$$\widehat{H}_{0,0} = \frac{\hbar^2}{\Delta r^2 m_0} + V_0$$
$$\widehat{H}_{n,n} = \frac{\hbar^2}{\Delta r^2 m_n} + V_n$$
$$\widehat{H}_{i,i} = \frac{\hbar^2}{4\Delta r^2}\left(\frac{1}{m_{i-1}} + \frac{2}{m_i} + \frac{1}{m_{i+1}}\right) + V_i$$
$$\widehat{H}_{i,i+1} = \frac{-\hbar^2}{4\Delta r^2}\left(\frac{1}{m_i} + \frac{1}{m_{i+1}}\right) \qquad \text{S7}$$
$$\widehat{H}_{i,i-1} = \frac{-\hbar^2}{4\Delta r^2}\left(\frac{1}{m_i} + \frac{1}{m_{i-1}}\right)$$

The output for this function is a diagonal matrix in which the eigenvectors are our electron/hole wavefunctions multiplied by their radius, as a function of the radius (r*$\psi(r)$) and our eigenvalues are the electron/hole energies. We can use this to plot our electron/hole wavefunctions for a variety of different core sizes and shell thicknesses.

Another experimentally verifiable output of these calculations is the bandgap. To predict a band gap, we used first order perturbation theory to calculate energy contributions from Coulombic interactions between the electron and hole:

$$E_c = \sum_{r=0}^{R} \frac{\left(\sum_{r'=0}^{r} |r' * \psi_e(r')|^2\right)\left(r * \psi_h(r)\right)^2 + \left(\sum_{r'=0}^{r} |r' * \psi_h(r')|^2\right)\left(r * \psi_e(r)\right)^2}{4\pi\epsilon_0 r \epsilon_r} \qquad \text{S8}$$

Finally, to obtain our bandgap, we subtracted this energy from the electron energy along with the hole energy (both of which were obtained as eigenvalues when calculating the $\widehat{H}$-matrix) as such:

$$Bandgap = E_{electron} - E_{hole} - E_c \qquad \text{S9}$$

These theoretical values are shown in Figure S12.

We also implemented a method to iteratively incorporate Coulombic potentials to produce wavefunctions that incorporate Coulombic attraction. In this method, we calculate the Coulombic energy caused by the interaction of the two particles on each other at every point in the radius of

the quantum dot. To do this, we first determine the charge density inside a given a point *r* along the radius:

$$E_{e(<r)} = \frac{q_e \sum_0^r |r' * \psi_e(r')|^2}{4\pi\epsilon_0 r \epsilon_r} \quad \text{S10}$$

$$E_{h(<r)} = \frac{q_e \sum_0^r |r' * \psi_h(r')|^2}{4\pi\epsilon_0 r \epsilon_r} \quad \text{S11}$$

We then determine the charge density outside a given a point *r* along the radius:

$$E_{e(>r)} = \sum_r^R \frac{q_e r' \left(\psi_e(r')\right)^2}{4\pi\epsilon_0 \epsilon_r} \quad \text{S12}$$

$$E_{h(>r)} = \sum_r^R \frac{q_e r' \left(\psi_h(r')\right)^2}{4\pi\epsilon_0 \epsilon_r} \quad \text{S13}$$

Adding both contributions gives its total Coulombic energy of the electron or hole at *r* and is added to the electron and hole potentials defined in our effective mass model (at each point *r*). Once this is done, we calculate the $\widehat{H}$-matrix of solutions to the Schrodinger equation again with the newly defined potentials. This process is repeated iteratively until the wavefunctions converge; we determine whether this has occurred by testing whether the band gap at each point has changed. Typically, three to five iterations are enough to produce convergence of the wavefunctions.

One of the more important applications of this model is to identify the electron/hole overlap (see Equation 2 from the main text). We must integrate the product of the wavefunctions (squared). Since our model is numerical however and solves for a finite number of points, we convert this into sum form to get the following:

$$\left|\int \psi_e(r)\psi_e(r)dr\right|^2 = \sum_{r=0}^{R} \psi_e(r_i)^2 * \psi_h(r_i)^2 * {r_i}^4 \qquad \text{S14}$$

Full PL lifetime decays

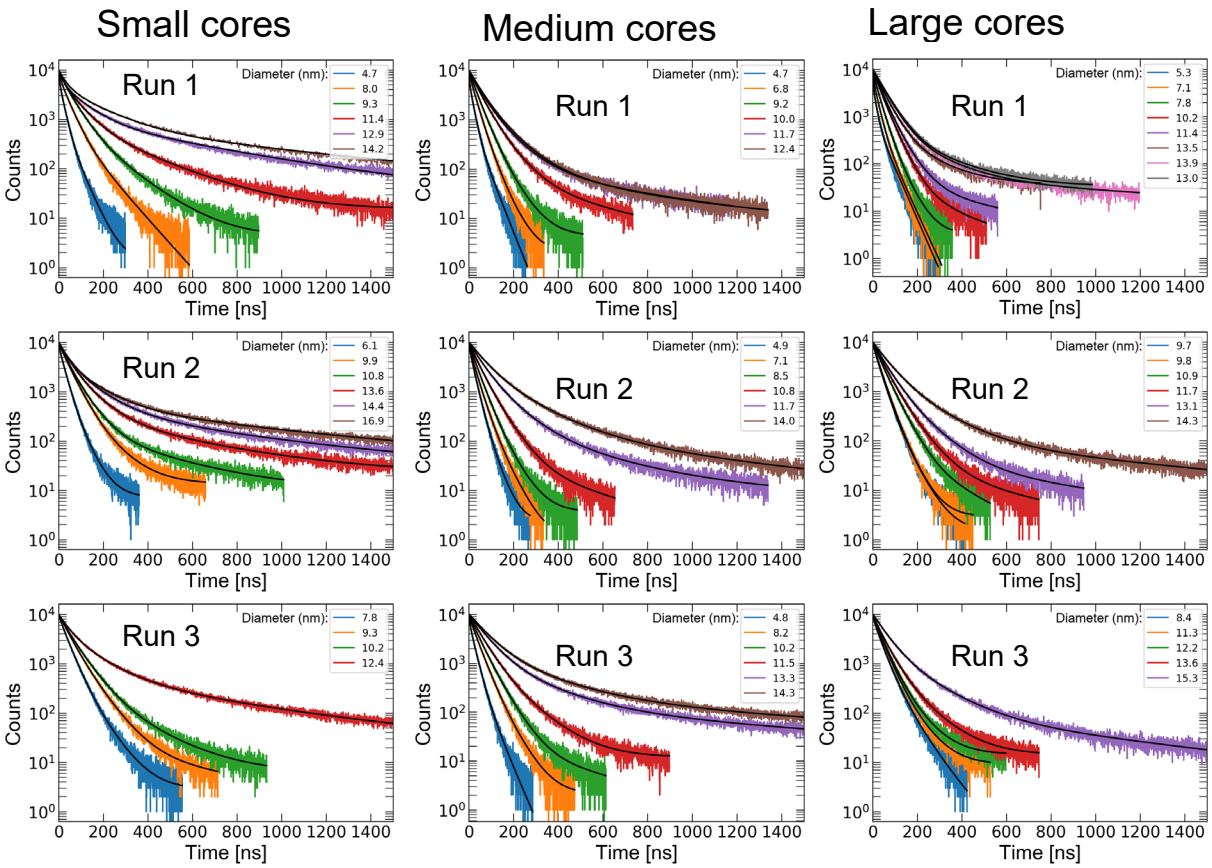

Figure S5. Time-resolved photoluminescence traces for all samples. Bi-exponential and tri-exponential fits are shown in black.

First decade PL lifetime decays

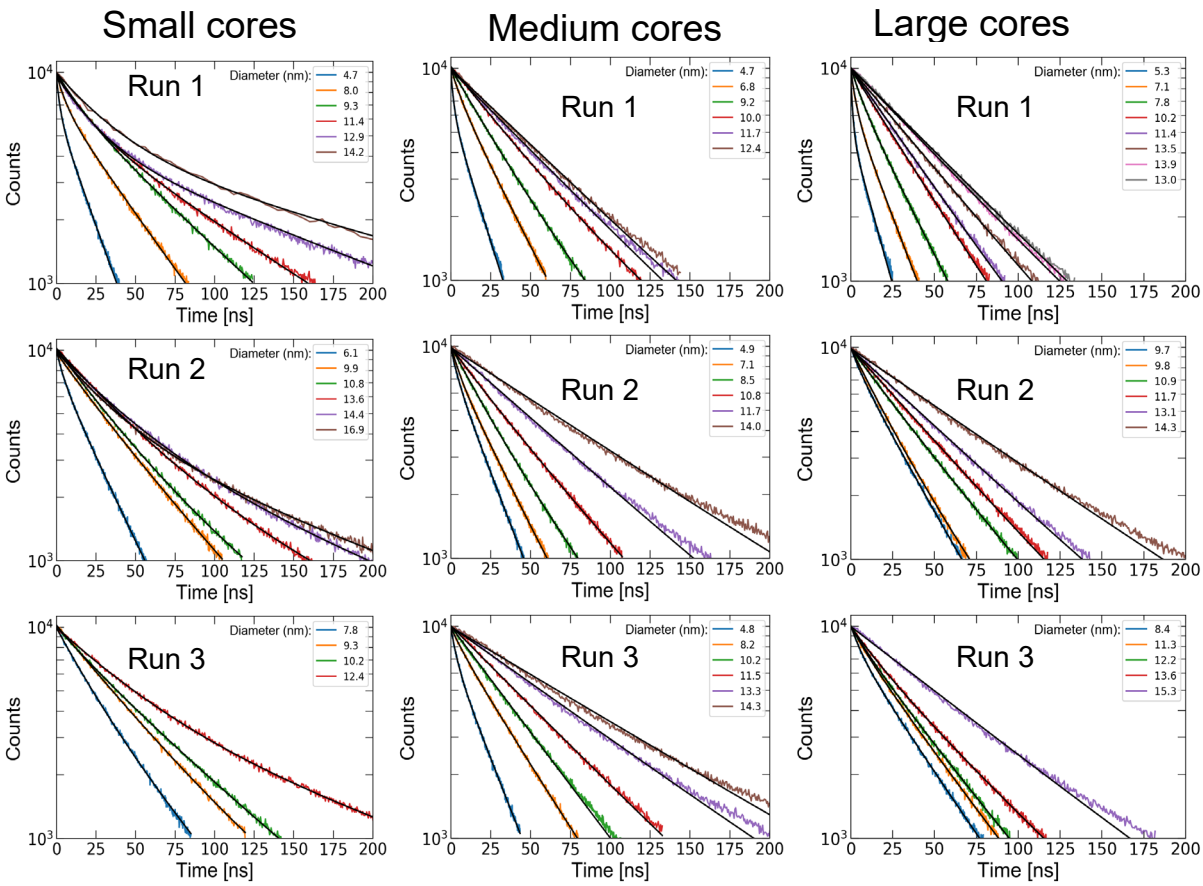

Figure S6. Time-resolved photoluminescence traces for all samples. Mono-exponential and bi-exponential fits are shown in black.

Radiative rates and lifetimes that incorporate quantum yields

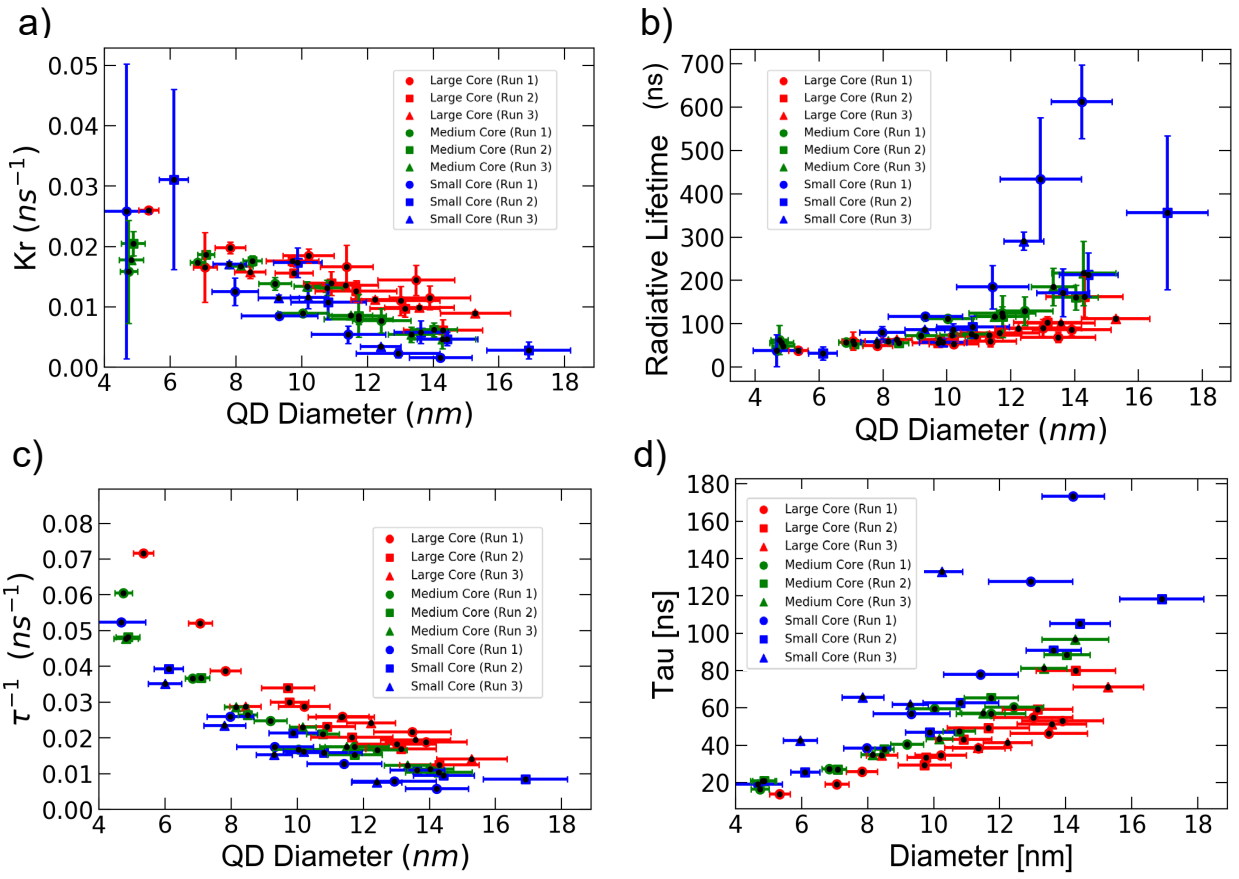

Figure S7. Radiative rates and lifetimes that incorporate photoluminescence quantum yield measurements in accordance with $k_r = \frac{PLQY}{\tau}$, where τ is the lifetime from the time-resolved photoluminescence data. The radiative rate, k_r, for all samples is shown (a), as well as the radiative lifetime, ${k_r}^{-1}$, for all samples (b). Rather large uncertainties in the quantum yields lead to large uncertainties in the rates. For comparison, the excited state recombination rate (τ^{-1}), and lifetime (τ) are shown (c,d). Plot (c) has the same data shown in the main text.

Comparing wavefunctions with and without Coulomb interaction

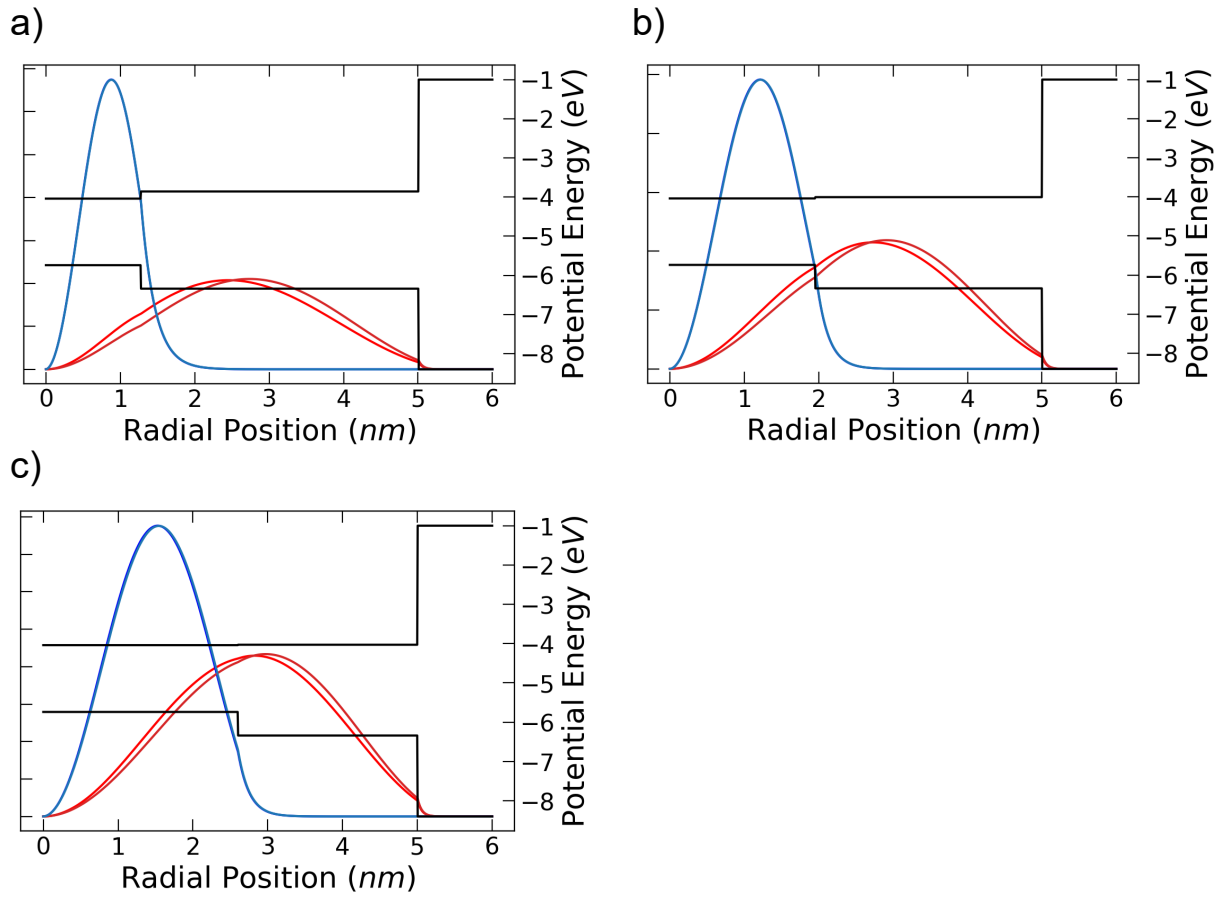

Figure S8. Hole (blue) and electron (red) radial probability functions, $|\psi_{e\ or\ h}(r)|^2 r^2$, that are computed without a Coulomb interaction potential (darker shade) and with a Coulomb interaction (brighter shade) for a few core/shell geometries with 10 nm total diameters and small cores (a), medium cores (b), and large cores (c). Inclusion of the Coulomb interaction does not appear to affect the hole wavefunctions, but does have a minor impact on the electron wavefunctions.

Effective mass model without Coulomb interaction

Electron and hole wavefunctions for variety of geometries (without Coulomb interaction)

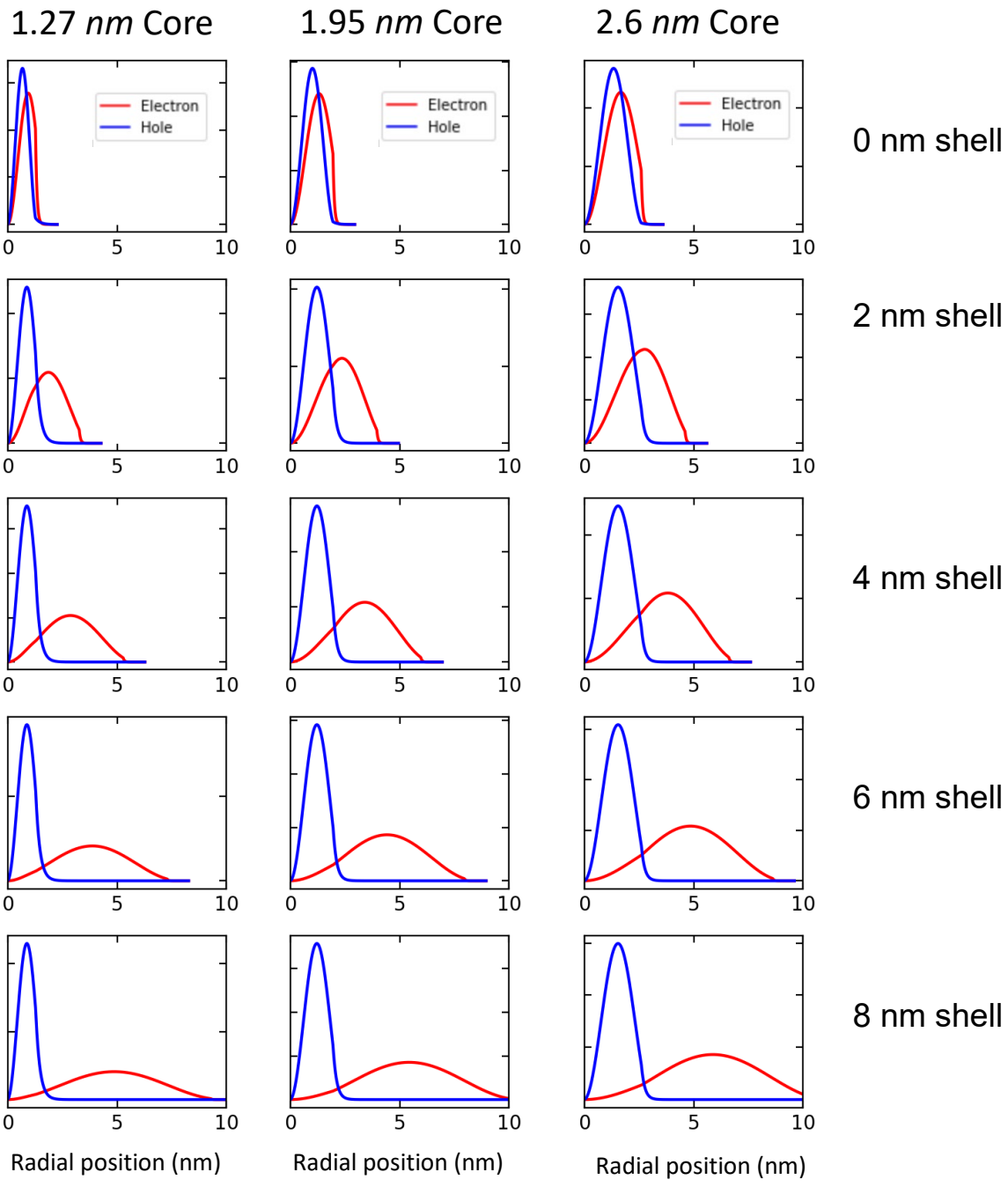

Figure S9. Hole (blue) and electron (red) radial probability functions, $|\psi_{e\ or\ h}(r)|^2 r^2$, that are computed without a Coulomb interaction potential for a few core/shell geometries.

Data analyzed with consistent conduction band offsets (without Coulomb interaction)

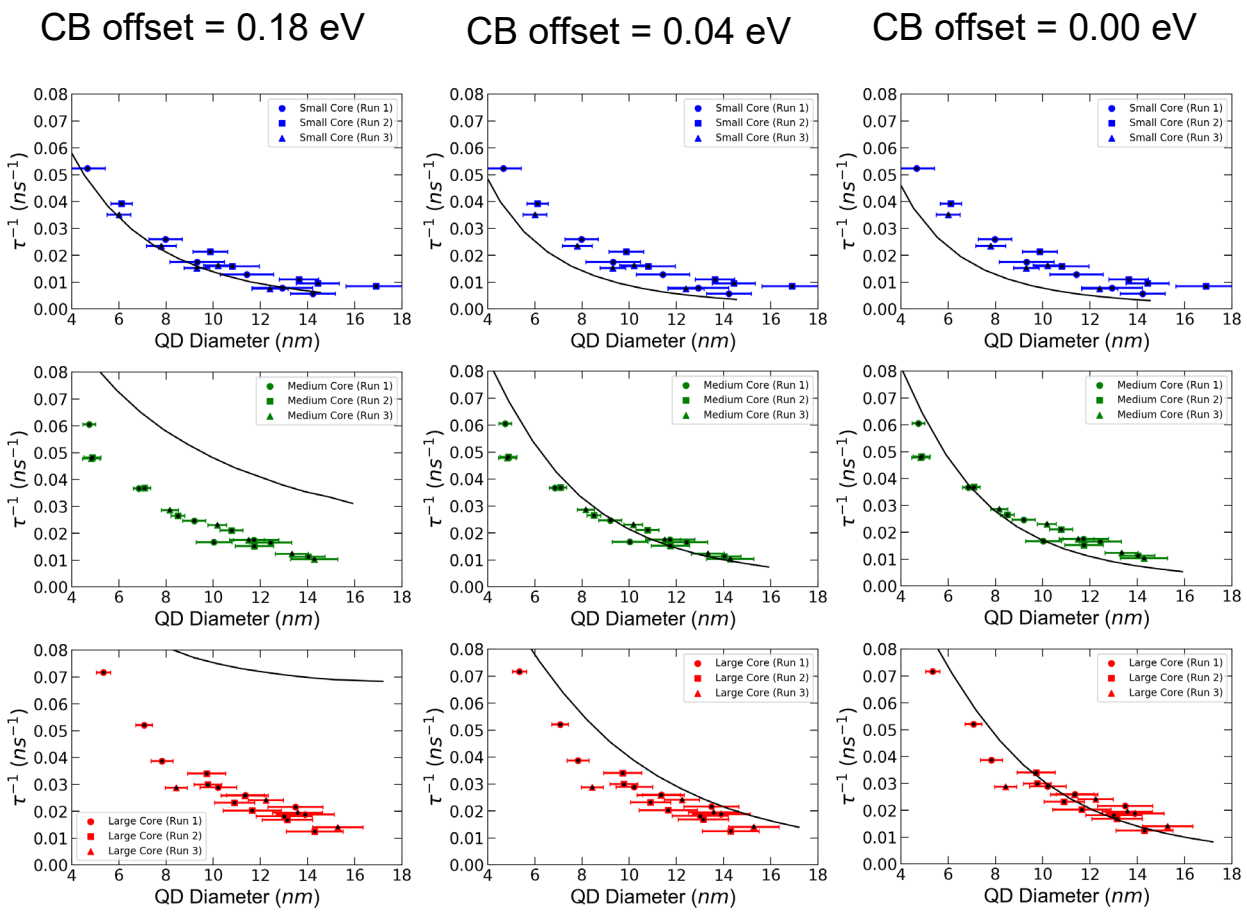

Figure S10. Experimental recombination rates for all three core sizes superimposed on simulated recombination rates from the effective mass model employing consistent conduction band offsets across all three core sizes. The left-most plots use CB offset = 0.18 eV, the middle plots use CB offset = 0.04 eV, and the right-most plots use CB offset = 0.0 eV. The pre-factor was set to C = 0.055 ns^{-1} eV^{-1}. Clearly there is no single value for CB offset that produces simulations that match data across all core sizes.

Contour plots of electron-hole overlap with consistent conduction band offsets (without Coulomb interaction)

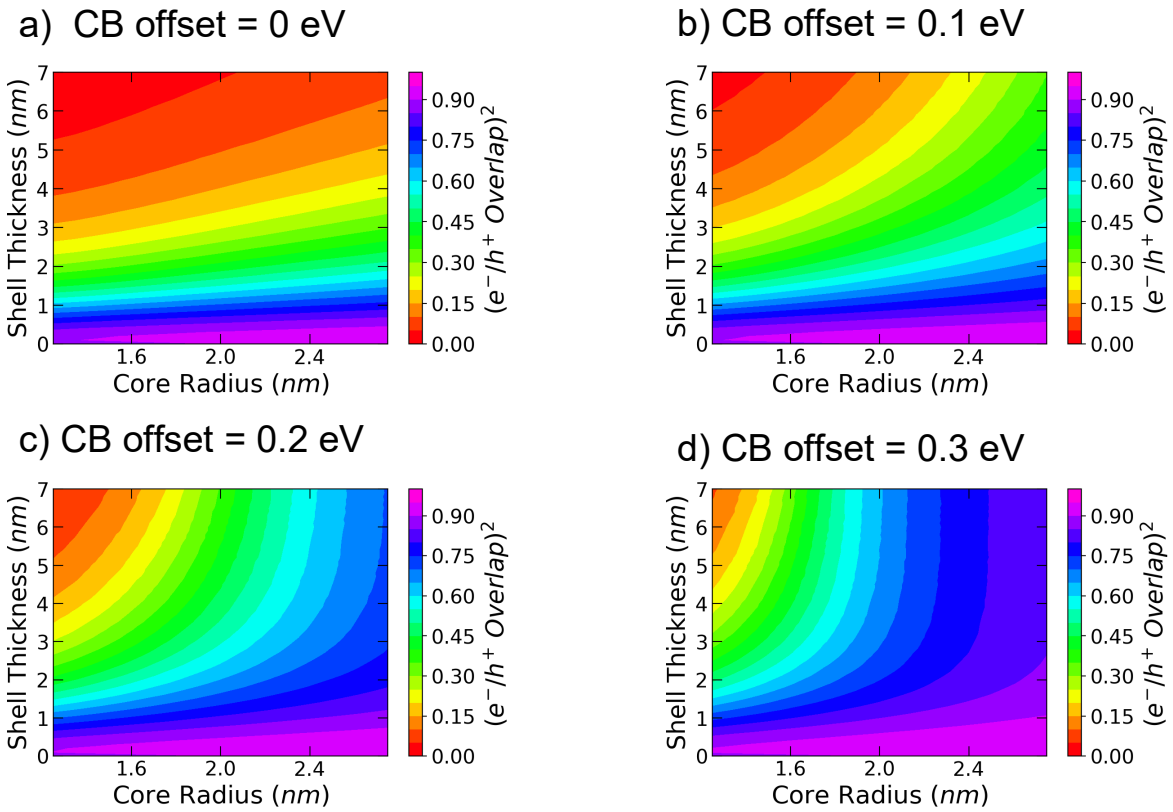

Figure S11. Contour plots of electron-hole overlap predicted from the effective mass model for four different values of the conduction band offset (and no Coulomb interaction). In each case, the CB offset is constant across all core sizes. The resultant plots predict a significant dependence of electron-hole overlap (and therefore radiative rate) on core size, while only a weak dependence is observed experimentally.

Geometry dependent bandgaps

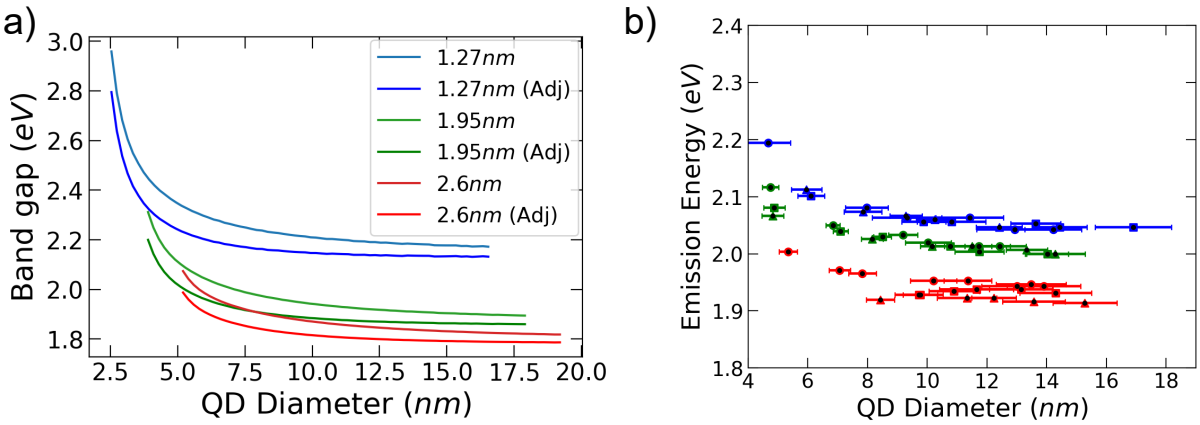

Figure S12. Band gaps were calculated using the effective mass model, with and without the Coulombic interaction energy (implemented via first order perturbation) (a). These predictions qualitatively agree with the experimental data of the geometry dependent emission energy (b).

Effective mass model with explicit Coulomb interaction

Electron and hole wavefunctions for a variety of geometries (with Coulomb interaction)

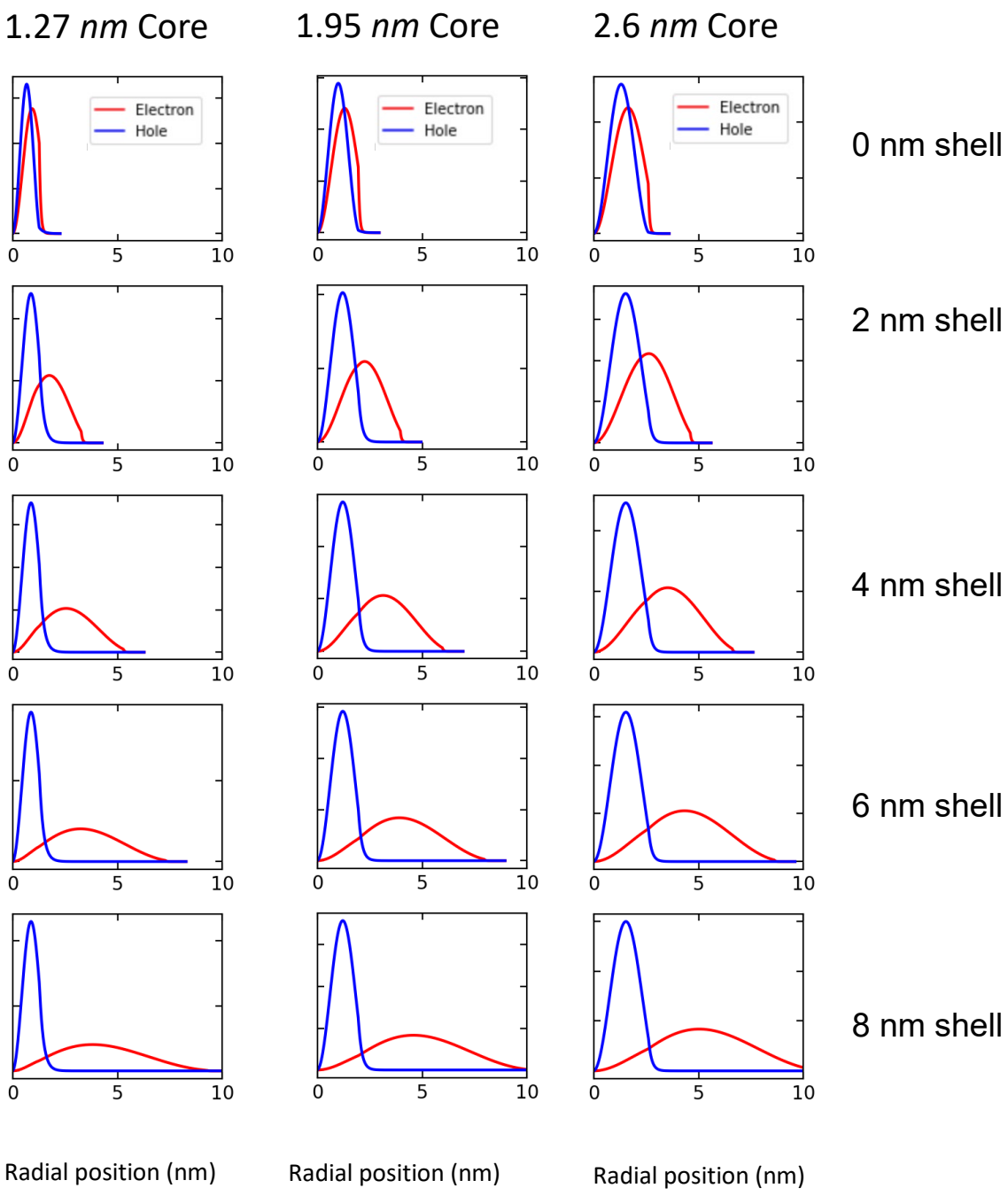

Figure S13. Hole (blue) and electron (red) radial probability functions, $|\psi_{e\ or\ h}(r)|^2 r^2$, that are computed with a Coulomb interaction potential for a few core/shell geometries.

Data analyzed with consistent conduction band offsets (with Coulomb interaction)

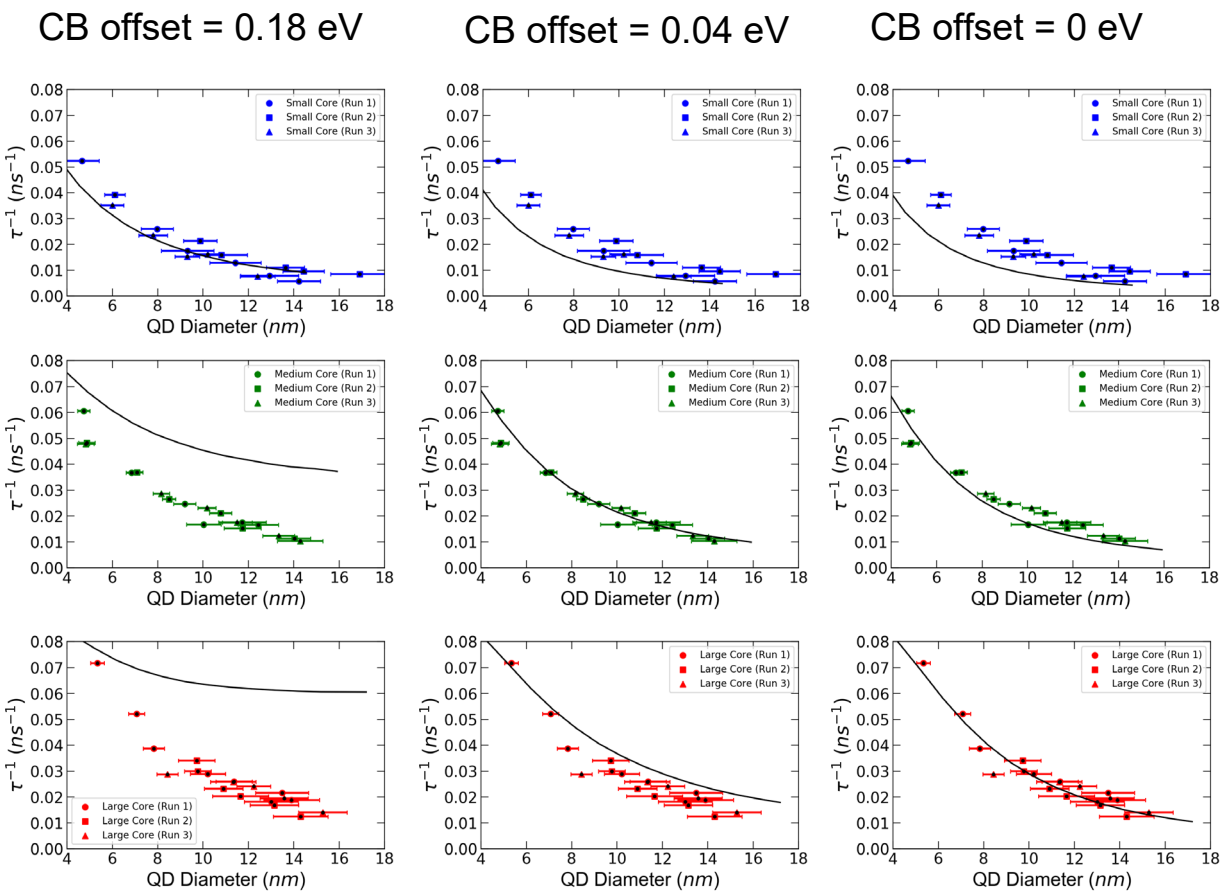

Figure S14. Experimental recombination rates for all three core sizes superimposed on simulated recombination rates from the effective mass model employing consistent conduction band offsets as well as an explicit coulombic interaction across all three core sizes. The left-most plots use CB offset = 0.18 eV, the middle plots use CB offset = 0.04 eV, and the right-most plots use CB offset = 0 eV. The pre-factor was set to C = 0.044 ns^{-1} eV^{-1}. Clearly there is no single value for CB offset that produces simulations that match data across all core sizes.

Contour plots of electron-hole overlap with consistent conduction band offsets (with Coulomb interaction)

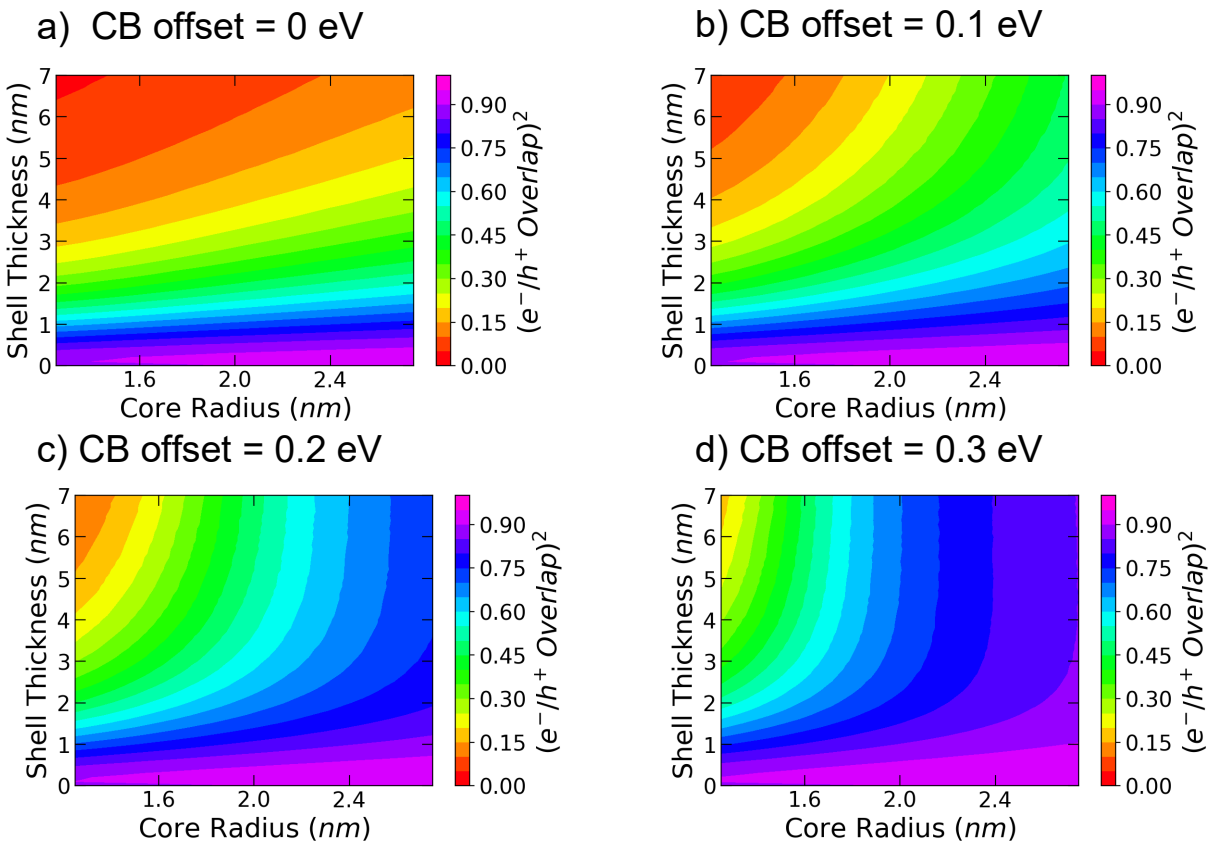

Figure S15. Contour plots of electron-hole overlap predicted from the effective mass model for four different values of the conduction band offset. In each case, the CB offset is constant across all core sizes and Coulombic interaction is explicitly accounted for in the model. The resultant plots predict a significant dependence of electron-hole overlap (and therefore radiative rate) on core size, while only a weak dependence is observed experimentally.

References

1 L. Carbone, C. Nobile, M. De Giorgi, F. D. Sala, G. Morello, P. Pompa, M. Hytch, E. Snoeck, A. Fiore, I. R. Franchini, M. Nadasan, A. F. Silvestre, L. Chiodo, S. Kudera, R. Cingolani, R. Krahne and L. Manna, *Nano Lett.*, 2007, **7**, 2942–2950.

3 J. Jasieniak, L. Smith, J. van Embden, P. Mulvaney and M. Califano, *J. Phys. Chem. C*, 2009, **113**, 19468–19474.

4 O. Chen, J. Zhao, V. P. Chauhan, J. Cui, C. Wong, D. K. Harris, H. Wei, H.-S. Han, D. Fukumura, R. K. Jain and M. G. Bawendi, *Nat. Mater.*, 2013, **12**, 445–451.

5 A. S. Powers, H.-G. Liao, S. N. Raja, N. D. Bronstein, A. P. Alivisatos and H. Zheng, *Nano Lett.*, 2017, **17**, 15–20.

6 N. D. Bronstein, Y. Yao, L. Xu, E. O'Brien, A. S. Powers, V. E. Ferry, A. P. Alivisatos and R. G. Nuzzo, *ACS Nano*, 2015, **2**, 1576–1583.

8 D. Schooss, A. Mews, A. Eychmüller and H. Weller, *Phys. Rev. B*, 1994, **49**, 17072–17078.

9 J. H. Olshansky, T. X. Ding, Y. V. Lee, S. R. Leone and A. P. Alivisatos, *J. Am. Chem. Soc.*, 2015, **137**, 15567–15575.

10 J. H. Olshansky, A. D. Balan, T. X. Ding, X. Fu, Y. V. Lee and A. P. Alivisatos, *ACS Nano*, 2017, **11**, 8346–8355.